Thermodynamic Properties, Shadows and Geodesic Motions of Quantum Corrected Spherically Symmetric AdS Black Hole with Phantom Global Monopoles

B. Hamil [1]

Universite Constantine 1 Faculte des Sciences Exactes, Laboratoire de Physique Mathématique et Subatomique, Constantine, 25000, Algeria

B. C. Lütfüoğlu [2]

Department of Physics, University of Hradec Kralove, Faculty of Science, Rokitanskeho 62, Hradec Kralove, Královéhradecký , 500 03, Czech Republic

F. Ahmed [3]

Department of Physics, University of Science & Technology Meghalaya, Ri-Bhoi, Meghalaya, 793101, India

Z. Yousaf [4]

Department of Mathematics, University of the Punjab, Quaid-i-Azam Campus, Lahore 54590, Pakistan

Abstract

In this paper, we introduce a metric ansatz for describing spherically symmetric quantum corrected black hole (BH) space-time within an AdS background, incorporating both ordinary and phantom global monopoles. Afterwards, we focus into the thermodynamic properties of this BH, calculating essential parameters such as the Hawking temperature and the specific heat capacity. Moving forward, we analyze the effective potential of the system for both null and time-like geodesics, as well as the shadow radius of the BH. Additionally, we compute the emission rate of particles from this BH. Finally, we explore the geodesic equations of motion and visualize the trajectories of massive particles within the BH. Throughout our investigation, we examine how the presence of ordinary and phantom global monopoles, alongside the quantum corrected parameter, influences various thermal properties, the effective potential of the system, the BH shadow radius, energy emission rate, and the trajectories of massive particles. Importantly, through the generation of figures depicting these phenomena, we highlight the distinctions between results obtained with ordinary global monopoles and phantom ones, across a range of quantum corrected parameter values considering small values of the energy scale parameter.

Keywords: Modified theories of gravity; global monopoles; thermal properties; shadows; geodesics.

PACS number(s): 04.20.Jb; 04.50.Kd; 51.30.+i; 67.80.Gb; 65.40.Ba; 65.40.Gr; 14.80.Hv; 98.62.Sb;

1 Introduction

Since the inception of general relativity, scientists have continuously explored avenues to modify gravity at its core. Among the myriad approaches, notable contenders include Lovelock gravity, Brane world cosmology, scalar-tensor theories, $f(\mathcal{R})$ gravity, $f(\mathcal{T})$ gravity, $f(\mathcal{G})$ gravity, $(\mathcal{R},\mathcal{T})$, $f(\mathcal{R},\mathcal{G})$ gravity etc. (see, for examples [1–7] and related references there in) and the intriguing concept of gravity's rainbow. Within this array of modifications to Einstein's gravity, gravity's rainbow emerges as a particularly promising candidate for addressing Ultraviolet divergences (UV).

[1] **hamilbilel@gmail.com**
[2] **bekir.lutfuoglu@uhk.cz (Corresponding author)**
[3] **faizuddinahmed15@gmail.com**
[4] **zeeshan.math@pu.edu.pk**

The investigation of gravitational waves (GWs) has played a pivotal role in cosmology and astrophysics since the formulation of the theory of general relativity in the 20th century. The Laser Interferometer Gravitational-Wave Observatory (LIGO) achieved a historic milestone by successfully detecting GW signals originating from binary BH mergers [8–11]. Subsequently, the LIGO/Virgo collaborations extended this achievement to encompass mergers involving BHs and neutron stars, ushering in a new era of multi-messenger astronomy. Notably, the emergence of GW signals from such events has spurred heightened interest in primordial BHs (PBHs) as they are posited to explain binary BH mergers.

It is worth mentioning that BH stand as a crucial entity in the realm of quantum gravity. Yet, the direct detection of four-dimensional BHs within particle accelerators remains an elusive pursuit. The staggering energy requirement, on the order of the Planck energy ($\sim 10^{19}$ GeV), exceeds current technological capabilities by a wide margin, dampening hopes of immediate observation. However, the prospect brightens in the presence of large extra dimensions. In such a scenario, the effective Planck scale can be lowered to the TeV range, rendering experiments feasible in the near future. Type I and Type II string theories are characterized by this reduction in the Planck scale, which is brought about by localizing standard model particles in the realms of the D-brane while allowing gravity to propagate freely in the higher-dimensional bulk [12]. Some recent investigations on BH physics can be found in [13–17].

The concept of obtaining a consistent quantum theory of gravity through BH thermodynamics has been proposed. Viewing the geometric aspects of BHs as thermodynamic variables offers a potent framework for constructing such a theory. Recognizing Bhs as thermodynamic entities has profoundly influenced our comprehension of gravitational theory and its interplay with quantum field theory. Recent advancements in gauge/gravity duality highlight the importance of thermodynamics for BHs [18–28]. Moreover, seminal works by Hawking and Page, which explored phase transitions of asymptotically AdS BHs [29], along with Witten's contributions on similar subjects [30], have further underscored the importance of BH thermodynamics. Various approaches, grounded in different ensembles, can be employed to study BH thermodynamics. For example, studying thermal stability within the canonical ensemble provides information about the sign of heat capacity, which controls whether BHs are thermally stable or unstable. The points of the phase transition and bound states are represented by the divergences of heat capacity and roots, respectively. Consequently, BH thermodynamics and their thermal stability have been extensively explored in the literature [31–35]. Pioneered by Bekenstein *et al.* [36, 37], the widely accepted theory states that BHs propagate as black bodies, with entropy being related to the horizon's area. The BHs, even ones considerably larger than the Planck scale, are now generally accepted to have entropy proportionate to their horizon area [36–41]. This prompts an intriguing question: When BHs shrink in size, what become the leading-order corrections?

Various attempts have been made to address this question. For example, utilizing a modified version of the asymptotic Cardy formula for BTZ, string-theoretic, and other BHs, whose microscopic degrees of freedom are described by an underlying Conformal Field Theory (CFT) [42], main modifications with logarithmic behavior have been revealed. Furthermore, taking matter fields into account in BH backgrounds results in logarithmic improvements to the entropy of BHs at the leading order [43–45]. Similarly, the leading-order correction to BH entropy is found to be logarithmic when considering the string-BH correspondence [46,47] and utilizing the Rademacher expansion of the partition function [48].

Investigations into the leading-order corrections to BH thermodynamics are currently of significant interest. Recent studies have explored the effects of quantum corrections on the thermodynamics and stability of various BHs reported in [49–54]. The corrected thermodynamics of dilatonic BHs have also been discussed, revealing a universal form of correction term [55]. Furthermore, investigations into the corrected thermodynamics of BHs from the perspective of partition functions have been conducted [48]. Quantum gravity effects on the thermodynamics and stability of Hořava-Lifshitz Bhs have been analyzed [56], as well as investigations into modified Hayward BHs, revealing correction terms that reduce pressure and internal energy [57].

The line-element describing a spherically symmetric BH with global monopoles (ordinary and phantom) in the spherical coordinates (t, r, θ, ϕ) is given by [58, 59]

$$ds^2 = -\mathcal{B}(r)\, dt^2 + \frac{dr^2}{\mathcal{B}(r)} + r^2\,(d\theta^2 + \sin^2\theta\, d\phi^2), \tag{1}$$

with the function

$$\mathcal{B}(r) = \Big(1 - 8\,\pi\,\eta^2\,\xi - \frac{2\,M}{r}\Big), \tag{2}$$

where η, M and ξ stands for the energy scale of symmetry breaking, the quantity of matter, and BH kinetic energy, respectively. The scenario mediated by $\xi = 1$ describes an arena of a regular global monopole that arises from the scalar field's non-negative and non-zero kinetic energy [60]. However, the phantom global monopole is generated by selecting -1 value of ξ, thereby relating it with the scalar field's negative kinetic energy.

On considering the quantum fluctuations associated with the spherically symmetric manifold, the corrections of 2D dilaton gravity theory can be observed mediated from the Einstein-Hilbert action accompanied by the 4D interaction theory [61]. Under such circumstances, it is feasible to renormalize a gravitational theory such as the 2D dilaton gravity, which was proposed by Kazakov and Solodukhin. In Ref. [62], authors presented a quantum-corrected Schwarzschild BH with an AdS background and investigated thermodynamics. The line-element describing this AdS background BH is given by

$$ds^2 = -f(r)\, dt^2 + f^{-1}(r)\, dr^2 + r^2\,(d\theta^2 + \sin^2\theta\, d\phi^2), \tag{3}$$

where

$$f(r) = \frac{1}{r}\,\sqrt{r^2 - \alpha^2} - \frac{2\,M}{r} + \frac{(r^2 - \alpha^2)^{3/2}}{r\,\ell^2}, \tag{4}$$

where $\Lambda = -\frac{3}{\ell^2}$ is the cosmological constant and $\alpha = 4\,\ell_p$ is a small correction that describes the behavior of spherical symmetric quantum fluctuations.

2 Quantum-corrected AdS BHs with phantom global monopoles

We aim to investigate a spherically symmetric AdS background BHs with phantom global monopoles (ordinary and phantom one) taking into account the quantum corrections. Therefore, we begin this section by introducing line-element ansatz of this spherically symmetric BHs in the coordinates (t, r, θ, ϕ) with ordinary and phantom global monopole taking into account the quantum correction given by

$$ds^2 = -\mathcal{F}(r)\, dt^2 + \frac{dr^2}{\mathcal{F}(r)} + r^2\,(d\theta^2 + \sin^2\theta\, d\phi^2). \tag{5}$$

where $\mathcal{F}$ is given by

$$\mathcal{F}(r) = \frac{1}{r}\,\sqrt{r^2 - \alpha^2} - \frac{2\,M}{r} - 8\,\pi\,\eta^2\,\xi + \frac{8\pi P (r^2 - \alpha^2)^{3/2}}{3r}\,, \tag{6}$$

with the thermodynamic pressure

$$P = \frac{3}{8\pi\ell^2}. \tag{7}$$

One can see that for zero quantum-correction parameter $\alpha \to 0$, $\ell \to \infty$, and $\xi = 1$, one we will find a space-time describing global monopole geometry which were obtained by Barriola *et al.* [60]. Moreover, for $\alpha \to 0$ and $\xi \to 0$, one will find a spherically symmetric AdS background BH or a space-time of Schwarzschild-AdS BH [29].

In this paper, our objective is to conduct a detailed investigation of spherically symmetric AdS background quantum-corrected BHs featuring both ordinary and phantom global monopoles. We structure our investigation as follows: Firstly, we study the thermodynamic properties of the quantum-corrected BHs and analyze the physical parameters associated with the system. Next, we analyze how the effective potential of the system and the shadows of BHs are influenced by the various parameters involved. Afterwards, we calculate the energy emission rate of the chosen BHs and illustrate graphically how ordinary and phantom global monopoles alter its value. Finally, we focus on the geodesic motions and discuss the trajectories of massive and light-like particles within this framework.

2.1 Thermodynamic analysis

At first, we attempt to obtain an analytic form of the event horizon by determining the roots of the lapse function.

$$\mathcal{F}(r)\Big|_{r=r_+} = 0. \tag{8}$$

However, we find from Eq. (6) that the following equation given by

$$\frac{1}{r_+}\sqrt{r_+^2 - \alpha^2} - \frac{2\,M}{r_+} - 8\,\pi\,\eta^2\,\xi + \frac{8\pi P(r_+^2 - \alpha^2)^{3/2}}{3r_+} = 0 \tag{9}$$

does not provide such an analytic solution and numerical methods must be employed. Next, using Eq. (9), we can express the BH mass in terms of the event horizon as follows:

$$M_H = \frac{r_+}{2}\left\{\sqrt{1-\left(\frac{\alpha}{r_+}\right)^2}\left[1+\frac{8\,\pi\,P\,r_+^2}{3}\left(1-\left(\frac{\alpha}{r_+}\right)^2\right)\right] - 8\,\pi\,\eta^2\,\xi\right\}. \tag{10}$$

Here, it is worth noting that for $\alpha = \eta = P = 0$, Eq. (10) reduces to the ordinary Schwarzschild BH mass, while for $\alpha = \eta = 0$ it shrinks to the AdS Schwarzschild BH mass [29]. Moreover, only in the absence of the quantum correction, Eq. (10) shortens to the AdS Schwarzschild BH mass with monopole

$$M_H = \frac{r_+}{2}\left(1 - 8\,\pi\,\eta^2\,\xi + \frac{8\,\pi\,P\,r_+^2}{3}\right). \tag{11}$$

Furthermore, for $\eta = 0$, it lessens to the quantum corrected-AdS Schwarzschild BH mass [63]. In Figure 1 we present the influence of the monopole term on the mass. In particular, we compare its effect in the absence and presence of the quantum correction.

In both scenarios, the BH mass increases for the phantom monopole which was already stated for the non-AdS BHs [58,59]. We also note that quantum corrections do not alter this effect except by setting a lower horizon bound on the mass due to the square root term. Then, we discuss that effect via different values of the correction term for three scenarios in Figure 2.

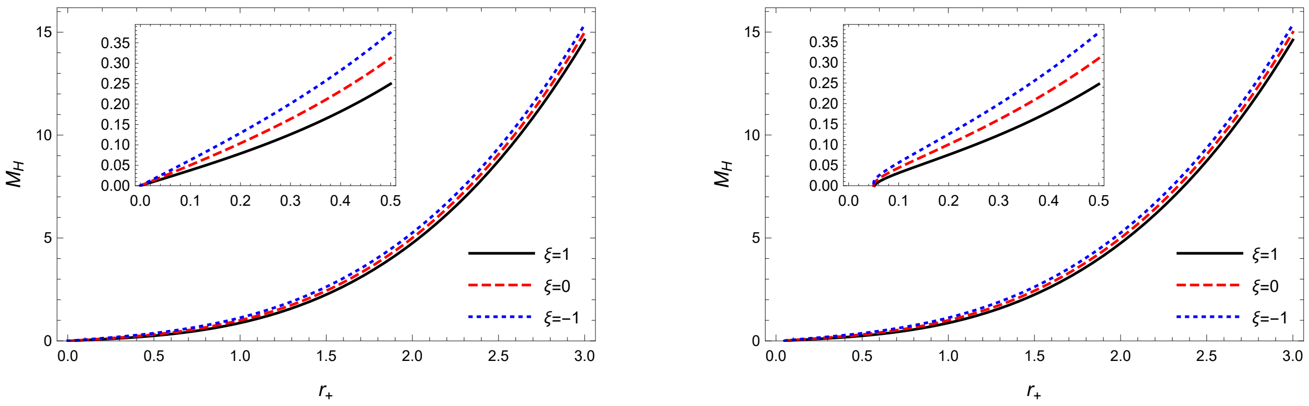

(a) $\alpha = 0$.   (b) $\alpha = 0.05$.

Figure 1: The qualitative representation of the mass function versus the horizon for $P = \frac{3}{8\pi}$ and $\eta = 0.1$.

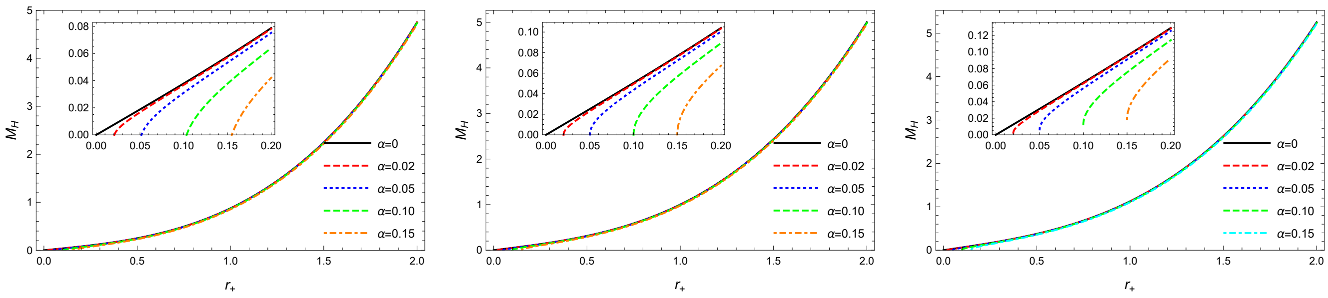

(a) $\xi = 1$.   (b) $\xi = 0$.   (c) $\xi = -1$.

Figure 2: The qualitative representation of the mass function versus the horizon in three different monopole scenarios for $P = \frac{3}{8\pi}$ and $\eta = 0.1$.

All cases show that the quantum effects solely modify the mass on the very small event horizons. Next, we derive the Hawking temperature by employing the formula

$$T_H = \frac{1}{4\pi} \frac{d\mathcal{F}}{dr}\bigg|_{r=r_+}. \tag{12}$$

Following the simple derivation, we obtain the Hawking temperature in the form of

$$T_H = \frac{1 + 8\pi P(r_+^2 - \alpha^2)}{4\pi\sqrt{r_+^2 - \alpha^2}} - \frac{2\eta^2\xi}{r_+}. \tag{13}$$

Like the mass, the Hawking temperature must have a real, thus, physical value. This fact implies that the event horizon of the BH has to meet the following condition

$$r_+ > \alpha. \tag{14}$$

Before proceeding to the graphical demonstration, we examine Eq. (13) in the $\alpha = \eta = P = 0$ and $\alpha = \eta = 0$ limits. We find that in both cases the ordinary Schwarzschild Hawking, $T_H = \frac{1}{4\pi r_+}$, and the AdS Schwarzschild Hawking temperatures, $T_H = \frac{1}{4\pi r_+} + 2Pr_+$, recover. Furthermore, in the absence of the quantum correction, Eq. (13) reduces to the AdS Schwarzschild BH mass with monopole

$$T_H = \frac{1}{4\pi r_+} + 2Pr_+ - \frac{2\eta^2\xi}{r_+}, \tag{15}$$

while in the absence of the monopole term, Hawking temperature turns to

$$T_H = \frac{1 + 8\pi P(r_+^2 - \alpha^2)}{4\pi\sqrt{r_+^2 - \alpha^2}}. \tag{16}$$

We see that the contribution of the monopole term to the Hawking temperature is articulated as a shift term that decreases or increases in proportion to the inverse of the event horizon. Now, we depict the Hawking temperature versus the event horizon to demonstrate the effects of the monopole and quantum corrections. Figure 3a shows the case without quantum correction corrections, while Figure 3b displays the case with the quantum corrections.

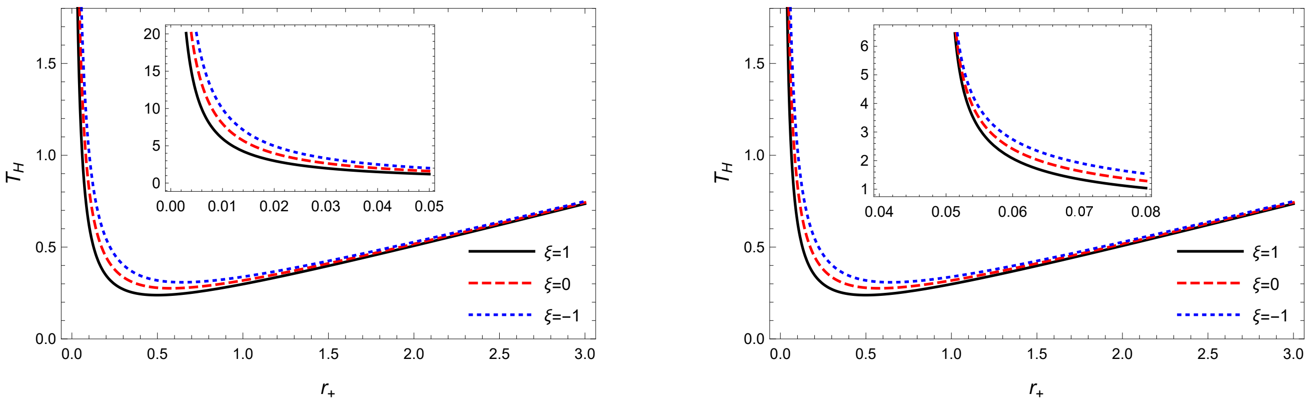

(a) $\alpha = 0$.

(b) $\alpha = 0.05$.

Figure 3: The qualitative representation of the Hawking temperature versus the horizon in three different monopole scenarios for $P = \frac{3}{8\pi}$ and $\eta = 0.1$.

In the quantum corrected case, we observe the lower bound of the event horizon. As a common behavior, we see that the Hawking temperature changes sharply in the presence of a monopole $\xi = 1$ in both cases. We then compare the impact of the quantum correction magnitude on three scenarios in Figure 4.

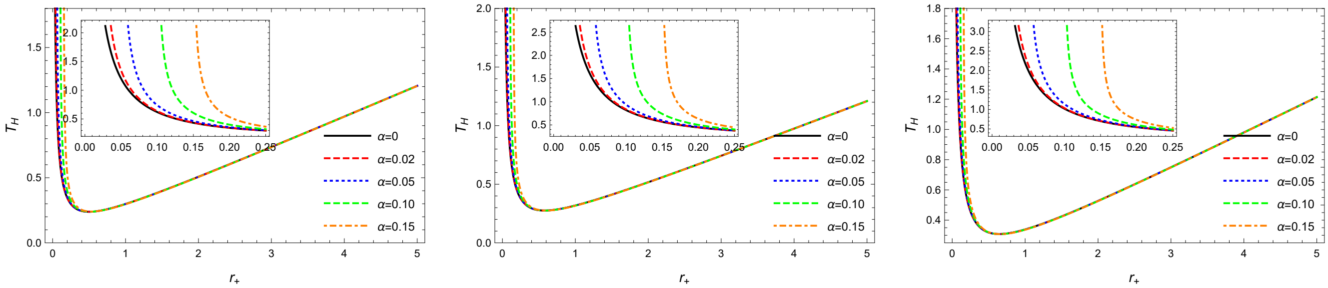

(a) $\xi = 1$.

(b) $\xi = 0$.

(c) $\xi = -1$.

Figure 4: The qualitative representation of the Hawking temperature versus horizon for in three different monopole scenarios $P = \frac{3}{8\pi}$, and $\eta = 0.1$.

In all three cases, we see that quantum corrections do not cause any change in large values of the event horizon. We now focus on the heat capacity function. To this end, we employ the following definition

$$C = \frac{dM}{dT}, \tag{17}$$

and using Eq. (17) we obtain the capacity as follows:

$$C = -2\pi r_+^2 \left(1-\frac{\alpha^2}{r_+^2}\right) \frac{1+8\pi P(r_+^2-\alpha^2)-8\pi\eta^2\xi\sqrt{1-\frac{\alpha^2}{r_+^2}}}{1-8\pi P(r_+^2-\alpha^2)-8\pi\eta^2\xi\sqrt[3]{1-\frac{\alpha^2}{r_+^2}}}. \tag{18}$$

We notice that for $\alpha = \eta = P = 0$, Eq.(18) diminishes to the conventional form of the specific heat function of the Schwarzschild BH, $C = -2\pi r_+^2$. Similarly, for $\alpha = \eta = 0$, Eq.(18) gives the heat capacity of the AdS Schwarzschild BH $C = -2\pi r_+^2 \frac{1+8\pi P r_+^2}{1-8\pi P r_+^2}$. Moreover, for $\eta = 0$, it lessens to the quantum corrected-AdS Schwarzschild BH heat capacity [63]

$$C = -2\pi r_+^2 \left(1-\frac{\alpha^2}{r_+^2}\right) \frac{1+8\pi P(r_+^2-\alpha^2)}{1-8\pi P(r_+^2-\alpha^2)}, \tag{19}$$

and similarly in the absence of quantum correction Eq.(18) reduces to

$$C = -2\pi r_+^2 \frac{1+8\pi P r_+^2-8\pi\eta^2\xi}{1-8\pi P r_+^2-8\pi\eta^2\xi}. \tag{20}$$

Here, we have to point out that the ordinary Schwarzschild BH differs from other scenarios in that it is unstable for all event horizon values. However, in other cases, for example in the AdS Schwarzschild BH scenario, the heat capacity is negative until $r_+ = \sqrt{\frac{1}{8\pi P}}$ and then positive. The existing discontinuity in that event horizon value indicates a second-order phase transition.

Now, we graphically demonstrate the impact of the monopole term on the heat capacity function in Figure 5.

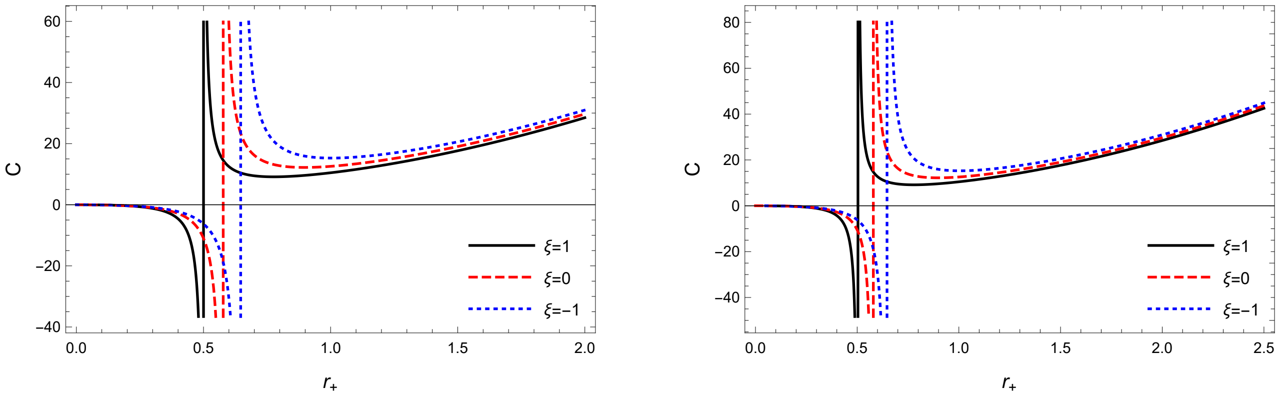

(a) $\alpha = 0$.

(b) $\alpha = 0.05$.

Figure 5: The qualitative representation of the heat capacity versus the horizon for $P = \frac{3}{8\pi}$ and $\eta = 0.1$.

The comparison of Figures 5a and 5b reveals a difference only in very small horizons where the BH is unstable. On the other hand, we note that both figures indicate the second-order phase transition occurrence in the greater horizon values for the phantom monopole scenarios.

We then display the impact of the quantum correction parameter in Figure 6.

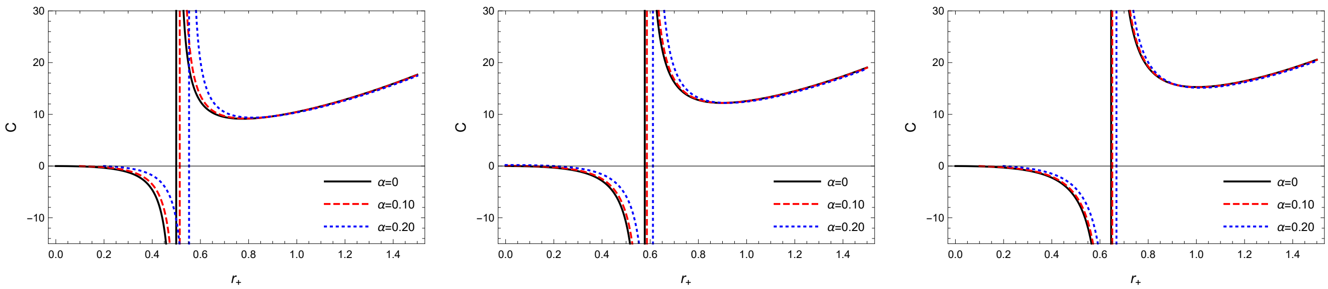

(a) $\xi = 1$. (b) $\xi = 0$. (c) $\xi = -1$.

Figure 6: The qualitative representation of the heat capacity versus horizon in three different monopole scenarios for $P = \frac{3}{8\pi}$, and $\eta = 0.1$.

We observe that in the greater quantum correction scenarios, the heat capacity function shifts slightly. Next, we derive the BH entropy by employing the customary definition, which is given in the form of

$$dS = \frac{dM}{T}. \tag{21}$$

After the integration, we find the entropy as

$$S \simeq \pi r_+^2 = \frac{A}{4}, \tag{22}$$

which does depend on neither quantum nor monopole corrections. Now, we derive the equation of state using Eq.(13). We find

$$P = -\frac{1}{8\pi\left(r_+^2 - \alpha^2\right)} + \frac{T_H}{2\sqrt{r_+^2 - \alpha^2}} + \frac{\eta^2 \xi}{r_+\sqrt{r_+^2 - \alpha^2}}. \tag{23}$$

We then depict pressure isotherms if Figure 7, and we compare the effects of the quantum corrections and monopole scenarios.

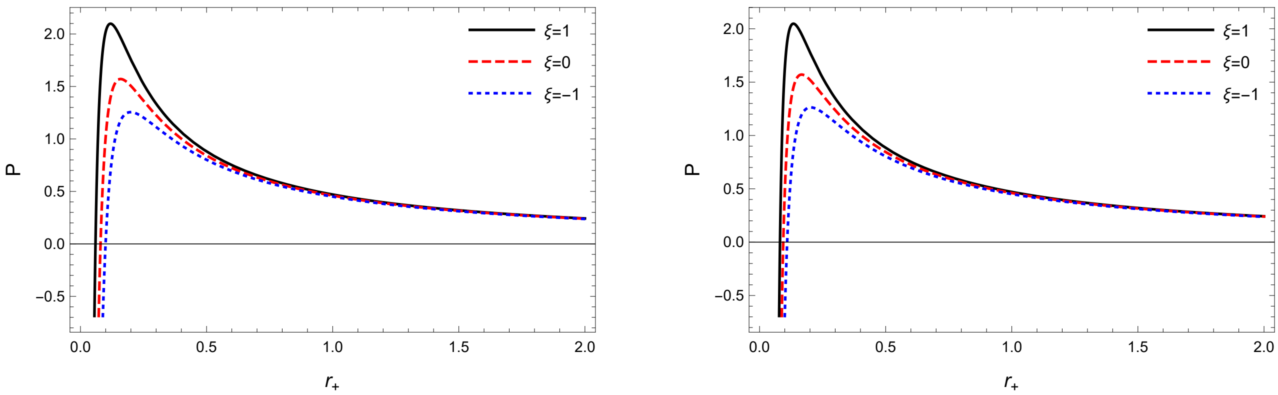

(a) $\alpha = 0$. (b) $\alpha = 0.05$.

Figure 7: The qualitative representation of the pressure isotherms versus the horizon for $T = 1$ and $\eta = 0.1$.

Figures 7a and 7b reveal that the pressure isotherms mimic itself including a shift on the event horizon lower bound. Here, we observe that the pressure peak occurs at a smaller pressure value and at a greater horizon in the phantom monopole case. We then depict Figure 8.

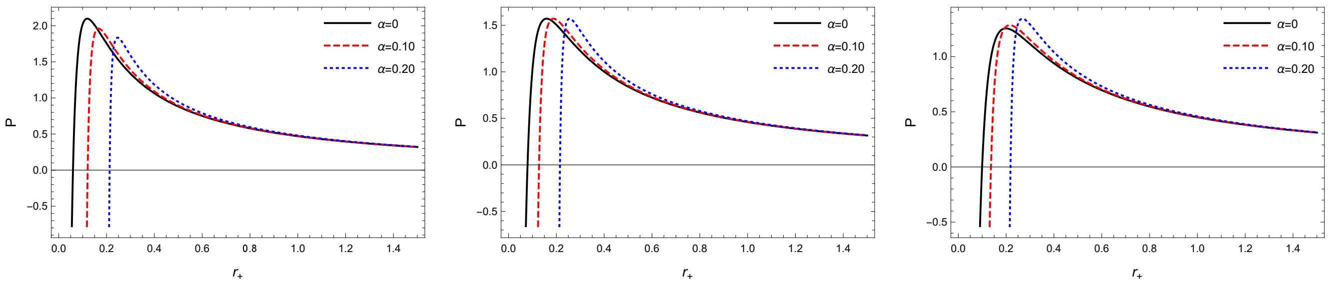

(a) $\xi = 1$. (b) $\xi = 0$. (c) $\xi = -1$.

Figure 8: The qualitative representation of the pressure isotherms versus horizon in three different monopole scenarios for $T = 1$, and $\eta = 0.1$.

We notice that the type of global monopole plays an important role. For example, in the ordinary global monopole case, we observe that as the α value increases, the maximal value of the pressure decreases. However, for the phantom global monopole case, we find that as the α value increases, the maximal value of the pressure also increases. Moreover, we note that if there is no monopole, the maximal value is not affected by the quantum corrections.

2.2 Effective potential of the system and Shadow behaviors

In this section, we analyze the effective potential of the system for both massive and massless particles within the chosen BH background (5). We investigate this using the Lagrangian method. According to this approach, the effective potential is defined as [64–70]

$$\mathcal{L} = \frac{1}{2}\, g_{\mu\nu}\, \dot{x}^{\mu}\, \dot{x}^{\nu}, \tag{24}$$

where dot represents ordinary derivative w. r. t an affine parameter of the curve, τ, and $g_{\mu\nu}$ is the metric tensor for the line-element (5).

Using the line-element (5) in the equatorial plane $\theta = \frac{\pi}{2}$, we obtain the following expression

$$\mathcal{L} = \frac{1}{2}\left[- \mathcal{F}(r)\, \dot{t}^2 + \mathcal{F}^{-1}(r)\, \dot{r}^2 + r^2\, \dot{\phi}^2 \right]. \tag{25}$$

One can see that the metric tensor $g_{\mu\nu}$ for the considered space-time is independent of (t, ϕ). Therefore, there are two constants of motions associated with these coordinates given by

$$-E = -\mathcal{F}(r)\, \dot{t} \Rightarrow \dot{t} = \frac{E}{\mathcal{F}(r)}, \tag{26}$$

$$L = r^2\, \dot{\phi} \Rightarrow \dot{\phi} = \frac{L}{r^2}, \tag{27}$$

where E is the conserved energy parameter, and L is the conserved z-component of the angular momentum.

With these, the Lagrangian (25) for light-like or time-like geodesics becomes

$$\left(\frac{dr}{d\tau}\right)^2 + \mathcal{F}(r)\left(- \epsilon + \frac{L^2}{r^2}\right) = E^2, \tag{28}$$

where $\epsilon = 0$ for null geodesics and -1 for time-like geodesics.

Eq. (28) can be seen as describing the dynamics of a classical particle of energy E subject to an effective potential given by

$$V_{eff}(r) = \left[\frac{1}{r}\sqrt{r^2-\alpha^2} - \frac{2\,M}{r} - 8\,\pi\,\eta^2\,\xi + \frac{(r^2-\alpha^2)^{3/2}}{r\,\ell^2}\right]\Big(-\epsilon + \frac{L^2}{r^2}\Big). \tag{29}$$

We've produced several graphs depicting the effective potential for null and time-like geodesics, factoring in both ordinary and phantom global monopoles across various values of the correction parameter α. In Figure 9, we plotted the effective potential for null geodesics considering the ordinary global monopole, while Figure 10 showcases the same for phantom global monopoles. We varied the angular momentum L across values of 1, 2, and 3 to observe its impact. Similarly, Figures 11 and 12 exhibit the effective potential for time-like geodesics. Again, we've explored different values of α while considering both ordinary and phantom global monopoles. In Figures 9 and 10, we have set $M = 0.1$, $P = \frac{3}{8\pi}$, $\eta = 0.1$, and $\epsilon = 0$, while in Figures 11 and 12, we choose $M = 0.1$, $P = \frac{3}{8\pi}$, $\eta = 0.1$ and $\epsilon = -1$.

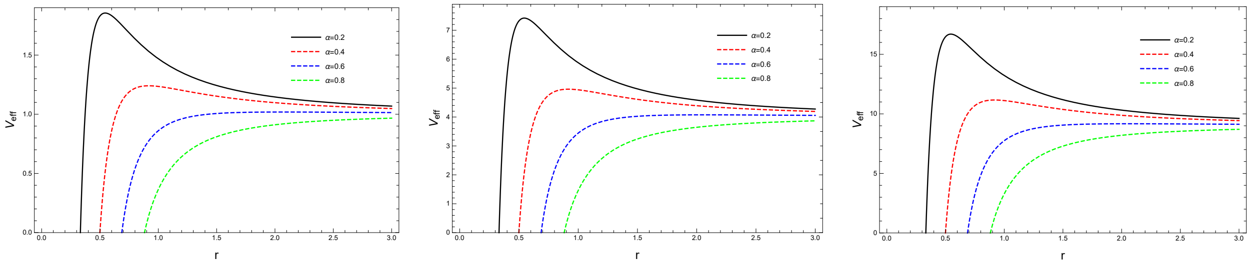

(a) $L = 1$. (b) $L = 2$. (c) $L = 3$.

Figure 9: The effective potential for null geodesics vs. r for different values of α. Here $\xi = 1$

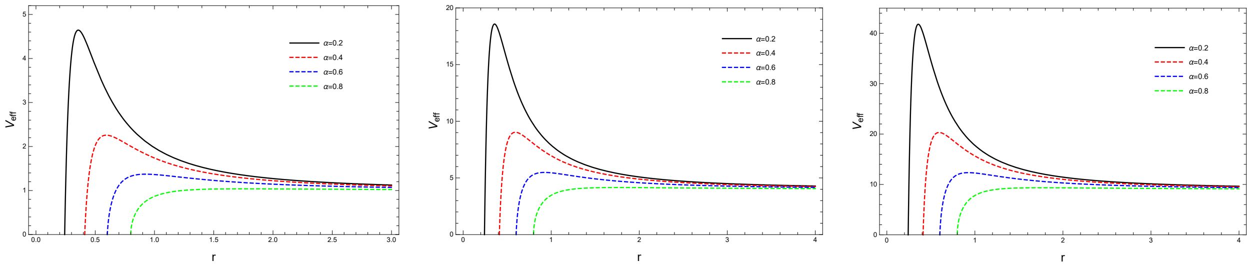

(a) $L = 1$. (b) $L = 2$. (c) $L = 3$.

Figure 10: The effective potential for null geodesics vs. r for different value of α. Here $\xi = -1$.

To examine the equation governing null geodesics in the spacetime of a deformed AdS BH with phantom global monopoles and analyzed how the Quantum correction affects the evolution of photons, we employ the Hamilton-Jacobi action,

$$\frac{\partial S}{\partial \tau} = -\frac{1}{2}g^{\mu\nu}\frac{\partial S}{\partial x^\mu}\frac{\partial S}{\partial x^\nu}, \tag{30}$$

where S is the Jacobi action.To examine the Hamilton-Jacobi equation, we adopt an ansatz in the following format:

$$S = \frac{m^2}{2}\tau - Et + L\phi + S_\theta\left(\theta\right) + S_r\left(r\right), \tag{31}$$

Here we set $m = \epsilon = 0$ for a photon. Using the conserved quantities E and L and inserting Eq. (31) into the Hamilton-Jacobi equation, Eq. (30), we find

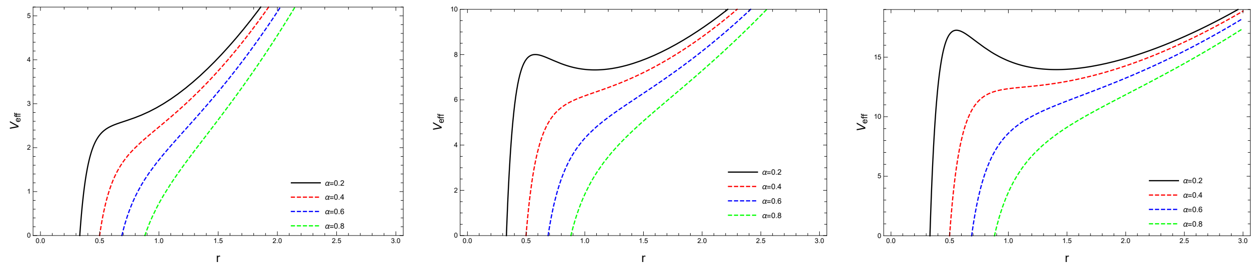

(a) $L = 1$. (b) $L = 2$. (c) $L = 3$.

Figure 11: The effective potential for time-like geodesics versus event horizon for different values of α for the usual global monopole case.

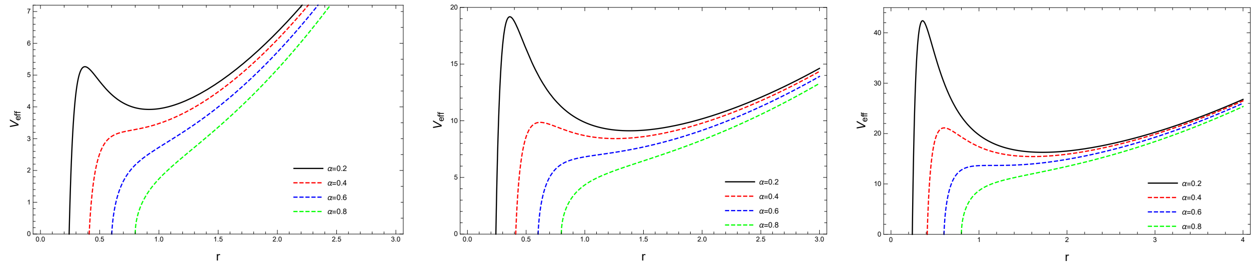

(a) $L = 1$. (b) $L = 2$. (c) $L = 3$.

Figure 12: The effective potential for time-like geodesics versus event horizon for different values of α for the phantom global monopole case.

$$r^2 \left(\frac{\partial S_r}{\partial r}\right)^2 = \frac{r^2 E^2}{\mathcal{F}^2(r)} - \frac{\left(L^2 + \mathcal{K}\right)}{\mathcal{F}(r)}. \tag{32}$$

$$\left(\frac{\partial S_\theta}{\partial \theta}\right)^2 = \mathcal{K} - L^2 \cot^2 \theta. \tag{33}$$

where $\mathcal{K}$ is called Carter's constant. By employing the subsequent definition of canonically conjugate momentum,

$$\frac{\partial S_\theta}{\partial \theta} = p_\theta = r^2 \frac{\partial \theta}{\partial \tau}, \tag{34}$$

and

$$\frac{\partial S_r}{\partial r} = p_r = \frac{1}{\mathcal{F}(r)} \frac{\partial r}{\partial \tau}, \tag{35}$$

we can obtain the null geodesic equations as follows:

$$r^2 \frac{\partial \theta}{\partial \tau} = \pm\sqrt{\Theta} = \sqrt{\mathcal{K} - L^2 \cot^2 \theta}, \tag{36}$$

$$r^2 \dot{r} = \pm\sqrt{\mathcal{R}} = \sqrt{r^4 E^2 - r^2 \mathcal{F}(r) \left(L^2 + \mathcal{K}\right)}. \tag{37}$$

Now, our attention shifts towards the radial equation as we introduce the potential.

$$\left(\frac{dr}{d\tau}\right)^2 + V\left(r\right) = 0, \tag{38}$$

where

$$V\left(r\right) = \left(L^2 + \mathcal{K}\right) \frac{\mathcal{F}(r)}{r^2} - E^2. \tag{39}$$

To discover the unstable circular orbits, we impose the following conditions

$$V(r)|_{r=r_p} = 0, \tag{40}$$

$$\left.\frac{\partial V(r)}{\partial r}\right|_{r=r_p} = 0, \tag{41}$$

and check that $\left.\frac{\partial^2 V(r)}{\partial r^2}\right|_{r=r_p} < 0$, where r_p is the radius of the photon sphere. Using the condition (40), leads

$$\beta + \delta^2 = \frac{r_p^2}{\frac{1}{r_p}\sqrt{r_p^2-\alpha^2} - \frac{2\,M}{r_p} - 8\,\pi\,\eta^2\,\xi + \frac{(r_p^2-\alpha^2)^{3/2}}{r_p\,\ell^2}}, \tag{42}$$

where we have applied the definitions of Chandrasekhar constants:

$$\beta = \frac{\mathcal{K}}{E^2} \text{ and } \delta = \frac{L}{E}. \tag{43}$$

The second condition (41) leads to

$$r_p \mathcal{F}'(r_p) - 2\mathcal{F}(r_p) = 0, \tag{44}$$

or

$$\frac{3\alpha^2 + 6M\sqrt{r_p^2-\alpha^2} - 8\pi\alpha^4 P + r_p^2\left(8\pi\alpha^2 P - 2\right) + 16\pi\eta^2\xi r_p\sqrt{r_p^2-\alpha^2}}{r_p\sqrt{r_p^2-\alpha^2}} = 0. \tag{45}$$

In this scenario, obtaining an exact solution for Eq. (45) is not feasible. Consequently, we opt for numerical methods for solving it. The presence of quantum correction and phantom global monopoles introduces 3-additional parameter, α, η and ξ, in Eq. (45). We explore various values for α, η and ξ and determine the photon sphere radius, r_p, by numerically solving Eq. (45). Subsequently, we calculate the values of $\beta + \delta^2$ in Tables 1 and 2.

To find the shape of the BH, we define and employ the following celestial coordinate system

$$X = \lim_{r_o\to\infty}\left(-r_o^2 \sin\theta_o \frac{d\phi}{dr}\right), \tag{46}$$

$$Y = \lim_{r_o\to\infty}\left(r_o^2 \frac{d\theta}{dr}\right). \tag{47}$$

Here r_o represents the distance from the BH to the observer's, θ_o, called the inclination angle, is the angle between the Black Hole's rotation axis and the observer's line of sight, and X measures the apparent perpendicular distance of the shadow from the symmetry axis, as seen by the observer, Y measures the apparent perpendicular distance of the shadow itself, as seen by the observer. By utilizing the equations that describe the null geodesics, we can derive the relationships between the celestial coordinate system and the impact parameters δ and β, which characterize the light ray trajectories. These relationships are expressed as follows:

$$X = -\frac{\delta}{\sin\theta_o}, \tag{48}$$

$$Y = \pm\sqrt{\beta - \delta^2 \cot^2\theta_o}. \tag{49}$$

In the equatorial plane ($\theta_o = \pi/2$), X and Y becomes

$$X = \delta \text{ and } Y = \sqrt{\beta}. \tag{50}$$

	$\eta = 0.1$		$\eta = 0.01$	
α	r_p	$\beta + \delta^2$	r_p	$\beta + \delta^2$
10^{-1}	4.09232	0.985601	3.05678	0.96612
5×10^{-2}	4.0281	0.984926	3.01974	0.964943
10^{-2}	4.00793	0.984705	3.00804	0.964561
5×10^{-3}	4.0073	0.984698	3.00768	0.964549
10^{-3}	4.0071	0.984696	3.00756	0.964545

Table 1: The values of photon radius, r_p, and impact parameters, for different values of α. We use $M = 1$, $P = \frac{3}{8\pi}$ and $\xi = 1$.

	$\eta = 0.1$		$\eta = 0.01$	
α	r_p	$\beta + \delta^2$	r_p	$\beta + \delta^2$
10^{-1}	2.42985	0.934713	3.04124	0.965616
5×10^{-2}	2.40549	0.932939	3.00455	0.964428
10^{-2}	2.39777	0.932365	2.99296	0.964042
5×10^{-3}	2.39753	0.932347	2.9926	0.964030
10^{-3}	2.39746	0.932341	2.99248	0.964026

Table 2: The values of photon radius, r_p, and impact parameters, for different values of α. We use $M = 1$, $P = \frac{3}{8\pi}$ and $\xi = -1$.

As a result, the Eq. (42) can be rewritten in the following form:

$$X^2 + Y^2 = \beta + \delta^2 = \frac{r_p^2}{\frac{1}{r_p}\sqrt{r_p^2 - \alpha^2} - \frac{2M}{r_p} - 8\pi\eta^2\xi + \frac{(r_p^2-\alpha^2)^{3/2}}{r_p\,\ell^2}} = R_s^2, \tag{51}$$

where R_s represents the radius of the BH's shadow. Figure 13 shows the variation of the shadow with quantum correction α, for two values of η. The plots are shown for both $\xi = +1, -1$ It is observed that R_s increases with the increase in quantum correction.

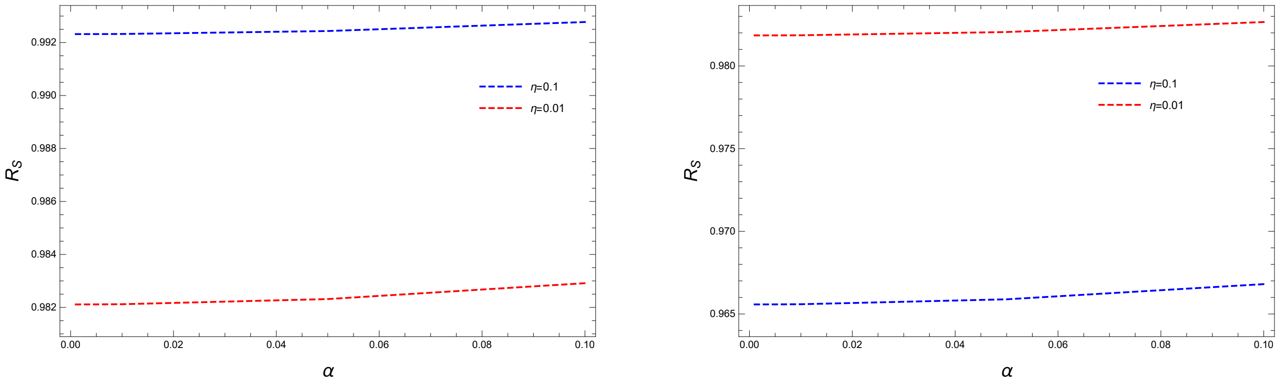

(a) Usual global monopole case.

(b) Phantom global monopole case.

Figure 13: Variation of the radius of BH shadow

2.3 Energy Emission Rate

It is known that, near the horizon quantum fluctuations lead to the creation and annihilation of particles. Through this process, particles with positive energy can tunnel out and escape from the BH's interior region, resulting in what is known as Hawking radiation. This Hawking radiation causes BHs to evaporate over time. In this section, we examine the associated rate of energy emission. For an observer located far away, the high-energy absorption cross-section approaches the BH's shadow. The absorption cross-section of the BH oscillates and converges to a limiting constant value σ_{lim} at high energies. This limiting constant value turns out to be approximately equal to the area of the photon sphere and can be expressed as

$$\frac{d^2E}{dtd\omega} = \frac{2\pi^2\sigma_{\text{lim}}}{e^{\frac{\omega}{T_H}} - 1}\omega^3. \tag{52}$$

Here ω represent the emission frequency, T_H is the Hawking temperature and σ_{lim} is the absorption cross-section, which is approximately equal to the geometrical cross-sectional area of the photon sphere

$$\sigma_{\text{lim}} \simeq \pi R_s^2. \tag{53}$$

Employing Eq. (53) into Eq. (52), we derive the black hole emission energy rate as

$$\frac{d^2E}{dtd\omega} = \frac{2\pi^3 R_s^2}{e^{\frac{\omega}{T_H}} - 1}\omega^3. \tag{54}$$

Figure (14) show the variation of energy emission rate with frequency ω for 3 values of α. The plots are shown for both $\xi = +1, -1$. We observe that all curves are coincide for both ordinary and phantom global monopoles. In Figure (15), we show the variation of the energy emission rate with frequency ω for both ordinary and phantom global monopoles with different values of $\alpha = 0.1,\ 0.01,\ 0.001$ considering small values of $\eta = 0.1$. We see that the energy emission rate varies for ordinary global monopole compared to phantom global monopole.

2.4 Geodesics Equations

Geodesics hold significant importance in physics, as they unveil the curvature of spacetime and the behavior of particles under gravitational forces. Understanding geodesics in the presence of quantum corrections can provide insights into how particles and fields behave at very small scales, where quantum effects become dominant. Furthermore, it is essential to understand the geodesic structure with quantum corrections present in order to interpret and analyze astrophysical observations associated with black holes, such as the characteristics of accretion disks and shadows. To examine the null and time-like geodesics of a test particle around the BH, we begin by establishing the geodesic equations along with their corresponding constraint equations,

$$\frac{d^2x^\beta}{d\tau^2} + \Gamma^\beta_{\mu\nu}\frac{dx^\mu}{d\tau}\frac{dx^\nu}{d\tau} = 0, \tag{55}$$

$$g_{\mu\nu}\frac{dx^\mu}{d\tau}\frac{dx^\nu}{d\tau} = \epsilon. \tag{56}$$

Here $\epsilon = 0$ and $\epsilon = -1$ correspond to null and time-like geodesics, respectively. For the metric (6), the geodesic equations take the following forms,

$$t''(\tau) = -\frac{r't'\left(3\left(\alpha^2 + 2M\sqrt{r^2-\alpha^2}\right) + 8\pi P\left(-\alpha^4 + 2r^4 - \alpha^2 r^2\right)\right)}{r\left(8\pi P r^4 - 3\alpha^2 - 6M\sqrt{r^2-\alpha^2} + 8\pi\alpha^4 P + r^2\left(3 - 16\pi\alpha^2 P\right) - 24\pi\eta^2\xi r\sqrt{r^2-\alpha^2}\right)}. \tag{57}$$

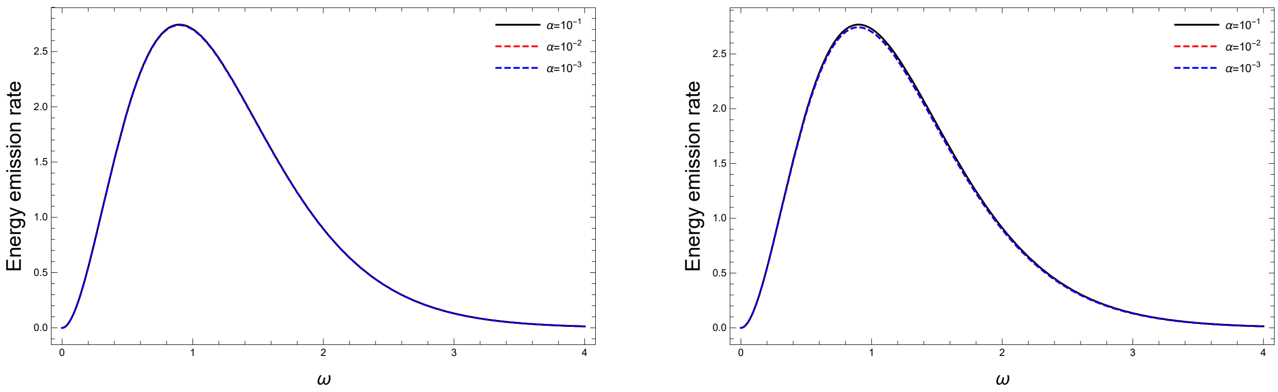

(a) $\xi = 1$.

(b) $\xi = -1$.

Figure 14: Energy emission rate behaviors for various values of the α parameter and $\eta = 0.01$

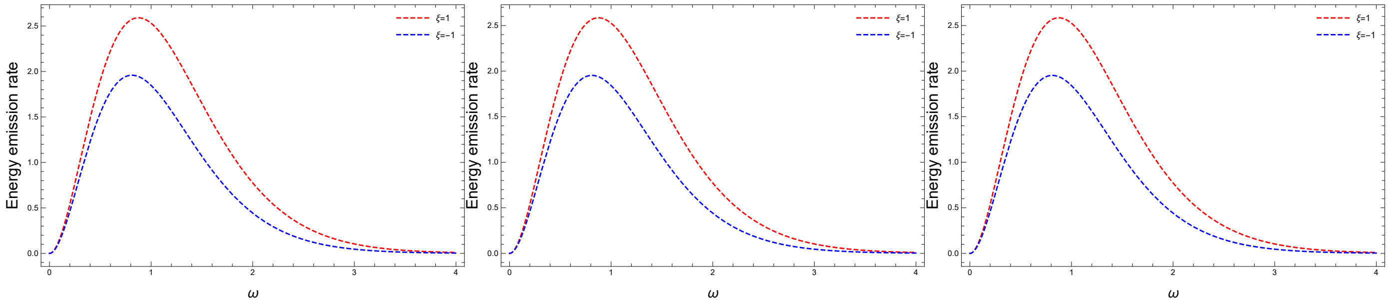

(a) $\alpha = 0.1$.

(b) $\alpha = 0.01$.

(c) $\alpha = 0.001$.

Figure 15: Energy emission rate behaviors for various values of the ξ parameter and $\eta = 0.1$

$$
\begin{aligned}
r''(\tau) = & -\frac{1}{18r^3\sqrt{r^2-\alpha^2}}\Big[t'^2\Big\{3(\alpha^2+2M\sqrt{r^2-\alpha^2})+8\pi P(-\alpha^4+2r^4-\alpha^2r^2)\Big\}\times \\
& \Big\{-6M+8\pi P\left(r^2-\alpha^2\right)^{3/2}+3(\sqrt{r^2-\alpha^2}-8\pi\eta^2\xi r)\Big\}\Big] \\
& +\left(\sin^2\theta\phi'^2-\theta'^2\right)\left(-2M+\frac{8\pi}{3}P\left(r^2-\alpha^2\right)^{3/2}+\left(\sqrt{r^2-\alpha^2}-8\pi\eta^2\xi r\right)\right) \\
& -\frac{r'^2\Big\{-3r\left(\alpha^2+2M\sqrt{r^2-\alpha^2}\right)-8\pi P(r^2-\alpha^2)(2r^3+\alpha^2 r)\Big\}}{2r^2\sqrt{r^2-\alpha^2}\Big\{-6M+8\pi P(r^2-\alpha^2)^{3/2}+3(\sqrt{r^2-\alpha^2}-8\pi\eta^2\xi r)\Big\}}.
\end{aligned} \tag{58}
$$

$$
\theta''(\tau) = \sin\theta\cos\theta\phi'^2 - \frac{2\theta' r'}{r}. \tag{59}
$$

$$
\phi''(\tau) = -\frac{2\phi'\left(r' + r\theta'\cot\theta\right)}{r}. \tag{60}
$$

It's clear that the equations above do not have analytical solutions, thus necessitating numerical analysis to investigate the trajectories of a test particle along geodesics. To achieve this, we use Mathematica code (Kerr Orbit GR Project), and we choose specific field parameters, such as θ, ϕ, then we proceed to solve for them. Initially, we provide initial conditions and solve for the coordinates parameterized with respect to τ. The Figure 16 is made with initial coordinates $x^\mu(0) = \left\{0, 4, \frac{\pi}{2}, \frac{\pi}{4}\right\}$ and different initial velocities. Notably, the energy scale of symmetry-breaking η, and kinetic energy ξ parameters have a significant impact on trajectories of massive particles, causing a contraction to it as η increases for fixed ξ. Furthermore, for $\xi = -1$, we observe that the event horizon expands as η decreases, while for $\xi = +1$, the event horizon expands as η increases. Figure 17 illustrates the behavior of trajectory photons. As expected, these particles also experience significant modifications compared to massive particles.

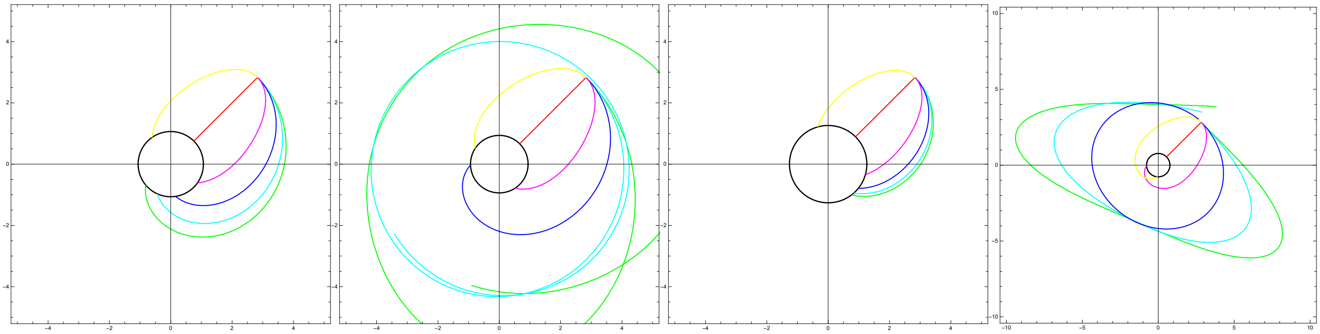

(a) $\xi = 1$ and $\eta = 0.1$. (b) $\xi = -1$ and $\eta = 0.1$. (c) $\xi = 1$ and $\eta = 0.2$. (d) $\xi = -1$ and $\eta = 0.2$.

Figure 16: trajectories of massive particles for slightly different initial velocities for $M = 1, P = \frac{3}{8\pi}, \alpha = 0.01$

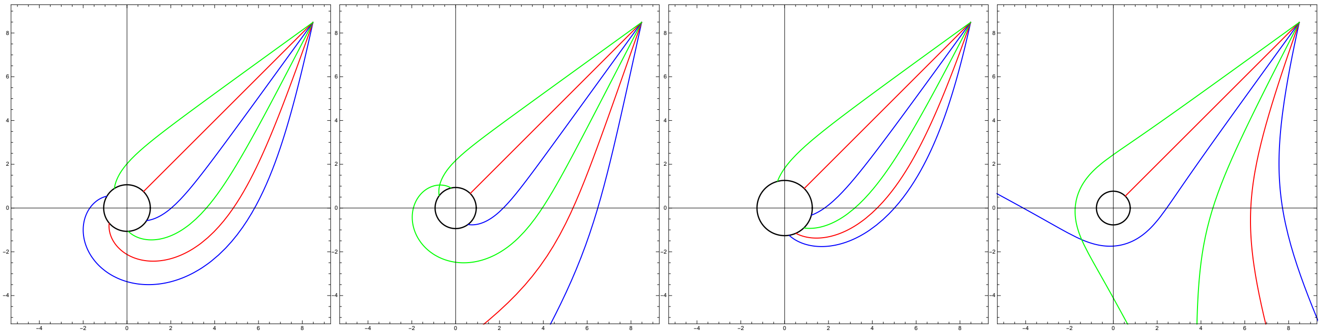

(a) $\xi = 1$ and $\eta = 0.1$. (b) $\xi = -1$ and $\eta = 0.1$. (c) $\xi = 1$ and $\eta = 0.2$. (d) $\xi = -1$ and $\eta = 0.2$.

Figure 17: Photon trajectories for slightly different initial velocities for $M = 1, r_0 = 0.05, P = \frac{3}{8\pi}, \alpha = 0.01$

3 Conclusions

The term "gravitational lensing" describes a group of phenomena that result from GR when a huge object's gravitational field bends and distorts the paths of light beams that are passing close by. The issue of BHs along with certain similar compact objects that can induce arbitrarily massive deflections is particularly noteworthy. Consequently, these deflections produce two infinite series of pictures of the same point of origin on opposite sides of the BH, where each image gets increasingly faint and gets closer to the edge of the shadow, a dark area. The analysis of such portraits has been the subject of much analytical and numerical research. This justifies our motivation to pursue work in this direction.

We now have an additional platform to test the fundamentals of gravity in the strong field region because of the latest results from the Event Horizon Telescope (EHT). The release of a collection of photos of our Milky Way's center BH and supermassive BH M87* is one of their most remarkable accomplishments. The powerful gravitational lensing of photons surrounding the BH is responsible for the dark patches in the center of the photographs. The shadow's radius is determined by the unstable photon orbit, also known as the photon sphere, located in the innermost layer surrounding the BH.

The bright rings shown in the photos correspond to the outer photon orbits. Additionally, the BH is constantly ignited by intricate accretion fluxes, which explains why the dazzling ring-shaped structure is the result of several light beams.

In this paper, we conducted a thorough investigation of spherically symmetric BHs featuring ordinary and phantom global monopoles within the framework of quantum-corrected proposals. Firstly, we examined the thermodynamic properties of the BHs under consideration, calculating the Hawking temperature and the heat capacity of the system. To illustrate the influences of various parameters, we generated several figures (Figures 1–8) for both ordinary and global monopoles, comparing our results with the case without these monopoles ($\xi = 0$).

Next, we analyzed the effective potential of the system for both ordinary and phantom global monopoles. We demonstrated that the effective potential for null geodesics differs between ordinary and phantom global monopoles. This discrepancy is also evident in the case of massive time-like geodesics. To visualize the effective potential for null and time-like geodesics, we generated Figures 9–12, depicting their behavior for different values of the quantum corrected parameter α, while setting the angular momentum values to $L = 1, 2, 3$ for both ordinary and phantom global monopoles. Additionally, Figure 13 illustrates the variation of the radius of the BH shadow. In Tables 1 and 2, we calculated a few values of the photon radius (r_p) and impact parameter ($\beta + \delta^2$) with different values of the quantum corrected parameter α, while considering $\eta = 0.1, 0.01$ for both ordinary and phantom global monopoles.

In addition, we computed the energy emission rate from the BHs under investigation. To delve deeper into this phenomenon, we depicted the emission rate with frequency ω in Figures 14–15 for various values of the quantum correction parameter α, considering both ordinary and phantom global monopoles. It becomes evident from these figures that the emission rates differ between these two types of monopoles.

Lastly, we investigated the geodesic equations of motion. To visually represent the trajectories of photons and massive particles, we created Figures 16–17, illustrating the effects of ordinary and phantom global monopoles for a constant value of the quantum corrected parameter α and the cosmological constant parameter ℓ.

Numerous studies have examined the phenomenon of photon deflection in diverse curved space-time backgrounds, including those generated by BHs, wormholes, and topological defects. These investigations have involved the thorough analysis of the impact of curvature on the angle of deflection experienced by null geodesics. In our future endeavour, we will focus on the deflection angle of photon rays in this BH model and show the influence of various factors, such as global monopoles, and quantum corrected parameter including the cosmological constant related with the parameter ℓ.

Despite the significant strides made in BH physics since the discoveries of BH thermodynamics and Hawking radiation, the pursuit of a unified theory of quantum gravity remains a formidable challenge. An exact derivation of Hawking effects in dynamic space-times eludes us, as does the generalization of thermodynamic laws to such contexts, grounded in fundamental principles. Various definitions of horizons and surface gravity have been proposed in the quest to generalize BH mechanics to dynamic cases, yet a debate persists regarding which horizon possesses thermodynamic characteristics and which surface gravity directly relates to the Hawking temperature. Additionally, each emitted Hawking particle contributes back to its source, triggering backreaction effects that continuously alter space-time dynamics. Our future efforts will be directed towards addressing these challenges.

Conflict of Interests

Authors declares no such conflict of interests.

Data Availability Statement

No data were generated or analyzed in this study.

Acknowledgements

F.A. acknowledges the Inter University Centre for Astronomy and Astrophysics (IUCAA), Pune, India for granting visiting associateship. B. C. L. is grateful to Excellence Project PřF UHK 2211/2023-2024 for the financial support.

References

[1] A. Malik, T. Naz, A. Qadeer, M. F. Shamir and Z. Yousaf, Eur. Phys. J. C **83**, 522 (2023).

[2] M. F. Shamir, A. Malik and G. Mustafa, Chin. J Phys. **73**, 634 (2021).

[3] D. Wang, M. Koussour, A. Malik, N. Myrzakulov and G. Mustafa, Eur. Phys. J. C **83**, 670 (2023).

[4] M. F. Shamir, G. Mustafa, S. Waseem and M. Ahmad, Commun. Theor. Phys. **73**, 115401 (2021).

[5] A. Malik, A. Shafaq, M. Koussour and Z. Yousaf, Eur. Phys. J. C **83**, 845 (2023).

[6] A. Malik, A. Shafaq, M. Koussour and Z. Yousaf, Eur. Phys. J. C **83**, 845 (2023).

[7] Z. Yousaf, K. Bamba, M. Z. Bhatti and U. Farwa, Int. J. Geom. Meth. Mod. Phys. (2024).

[8] B. P. Abbott *et al.* (LIGO Scientific, Virgo), Phys. Rev. Lett. **116**, 241103 (2016).

[9] B. P. Abbott *et al.* (LIGO Scientific, Virgo), Phys. Rev. Lett. **116**, 061102 (2016).

[10] B. P. Abbott *et al.* (LIGO Scientific, Virgo), Phys. Rev. Lett. **119**, 141101 (2017).

[11] B. P. Abbott *et al.* (LIGO Scientific, Virgo), Phys. Rev. Lett. **119**, 161101 (2017).

[12] N. Arkani-Hamed, S. Dimopoulos and G. Dvali, Phys. Lett. B **429**, 263 (1998).

[13] P. K. Dahal, F. Simovic, I. Soranidis and D. R. Terno, Phys. Rev. D **108**, 104014 (2023).

[14] S. Di Gennaro, Y. C. Ong, Phys. Lett. B **829**, 137112 (2022).

[15] H. C. D. Lima Junior, L. C. B. Crispino, P. V. P. Cunha, C. A. R. Herdeiro, Phys. Rev. D **103**, 084040 (2021).

[16] N. Dorey, R. Mouland and B. Zhao, JCAP 08 (**2021**) 036.

[17] N. Dorey, R. Mouland and B. Zhao, J. High Energ. Phys. **2023**, 166 (2023).

[18] E. Witten, Adv. Theor. Math. Phys. **2**, 253 (1998).

[19] O. Aharony, S. S. Gubser, J. M. Maldacena, H. Ooguri and Y. Oz, Phys. Rep. **323**, 183 (2000).

[20] O. Aharony, O. Bergman, D. L. Jafferis, J. M. Maldacena, J. High Energy Phys. **10**, 091 (**2008**).

[21] D. A. Lowe, Phys. Rev. **D 79**, 106008 (2009).

[22] J. Jing, S. Chen, Phys. Lett. B **686**, 68 (2010).

[23] Y. P. Hu, P. Sun, J.H. Zhang, Phys. Rev. D **83**, 126003 (2011).

[24] X. O. Camanho, J. D. Edelstein, J. High Energy Phys. **04**, 007 (**2010**).

[25] Y. P. Hu, H. F. Li, Z. Y. Nie, J. High Energy Phys. **01**, 123 (**2011**).

[26] J. Jing, Q. Pan, S. Chen, J. High Energy Phys. **11**, 045 (**2011**).

[27] D. Bazeia, L. Losano, G. J. Olmo, D. Rubiera-Garcia, Phys. Rev. **D 90**, 044011 (2014).

[28] D. Kabat, G. Lifschytz, J. High Energy Phys. **09**, 077 (**2014**).

[29] S. W. Hawking, D. N. Page, Commun. Math. Phys. **87**, 577 (1983).

[30] E. Witten, Adv. Theor. Math. Phys. **2**, 505 (1998).

[31] Y. S. Myung, Phys. Rev. **D 77**, 104007 (2008).

[32] D. Kastor, S. Ray, J. Traschen, Class. Quantum Gravity **26**, 195011 (2009).

[33] F. Capela, G. Nardini, Phys. Rev. **D 86**, 024030 (2012).

[34] S. H. Hendi, S. Panahiyan, Phys. Rev. **D 90**, 124008 (2014).

[35] A. Perez, M. Riquelme, D. Tempo, R. Troncoso, J. High Energy Phys. **2015**, 161 (2015).

[36] J. D. Bekenstein, Phys. Rev. **D 7**, 2333 (1973).

[37] S. W. Hawking, Phys. Rev. **D 13**, 191 (1976).

[38] A. Strominger, C. Vafa, Phys. Lett. **B 379**, 99 (1996).

[39] A. Ashtekar, J. Baez, A. Corichi, K. Krasnov, Phys. Rev. Lett. **80**, 904 (1998).

[40] S. Carlip, Phys. Rev. Lett. **82**, 2828 (1999).

[41] S. N. Solodukhin, Phys. Lett. **B 454**, 213 (1999).

[42] S. Carlip, Class. Quantum Grav. **17**, 4175 (2000).

[43] A. J. M. Medved, G. Kunstatter, Phys. Rev. **D 63**, 104005 (2001).

[44] A. J. M. Medved, G. Kunstatter, Phys. Rev. **D 60**, 104029 (1999).

[45] R. B. Mann, S. N. Solodukhin, Nucl. Phys. **B 523**, 293 (1998).

[46] S. N. Solodukhin, Phys. Rev. **D 57**, 2410 (1998).

[47] J. Sadeghi, B. Pourhassan, F. Rahimi, Can. J. Phys. **92**, 1638 (2014).

[48] D. Birmingham, S. Sen, Phys. Rev. **D 63**, 047501 (2001).

[49] A. Pourdarvish, J. Sadeghi, H. Farahani, B. Pourhassan, Int. J. Theor. Phys. **52**, 3560 (2013).

[50] S. Upadhyay, B. Pourhassan, H. Farahani, Phys. Rev. **D 95**, 106014 (2017).

[51] B. Pourhassan, H. Farahani, S. Upadhyay, Int. J. Mod. Phys. **A 34**, 1950158 (2019).

[52] B. C. Lütfüoğlu, B. Hamil, L. Dahbi, Int. J. Mod. Phys. A **37**, 2250126 (2022).

[53] H. Chen, H. Hassanabadi, B. C. Lütfüoğlu, Z. W. Long, Gen. Relativ. Gravit. **54**, 143 (2022).

[54] B.Hamil, B. C. Lütfüoğlu, Phys. Dark Universe **42**, 101293 (2023).

[55] J. Jing, M. L. Yan, Phys. Rev. **D 63**, 024003 (2001).

[56] B. Pourhassan, S. Upadhyay, H. Saadat, H. Farahani, Nucl. Phys. **B 928**, 415 (2018).

[57] B. Pourhassan, M. Faizal, U. Debnath, Eur. Phys. J. C **76**, 145 (2016).

[58] S. Chen, J. Jing, Class. Quantum Grav. **30**, 175012 (2013).

[59] M. Sharif, S. Iftikhar, Adv. High Energy Phys. **2015**, 854264 (2015).

[60] M. Barriola, A. Vilenkin, Phys. Rev. Lett. **63**, 341 (1989).

[61] D. I. Kazakov, S. N. Solodukhin, Nucl. Phys. **B 429**, 153, (1994).

[62] S. Wu, C. Liu, Nucl. Phys. B **985**, 115987 (2022).

[63] B. Hamil, B. C. Lütfüoğlu, L. Dahbi, arXiv:2307.16287 [gr-qc].

[64] F. Ahmed, Adv. High Energy Phys. **2017**, 3587018 (2017).

[65] F. Ahmed, Prog. Theor. Exp. Phys. **2017**, 083E03 (2017).

[66] F. Ahmed, F. Rahaman, Adv. High Energy Phys. **2018**, 7839619 (2018).

[67] F. Ahmed, F. Rahaman, Eur. Phys. J **A 54**, 52 (2018).

[68] F. Ahmed, EPL **142**, 39002 (2023).

[69] F. Ahmed, Int. J. Geom. Meths. Mod. Phys. (2024) 2450187.

[70] B. Hamil, B.C. Lütfüoğlu, Phys. Dark Universe **44** 101484 (2024).